Journal of Power Sources 184 (2008) 456–461

Contents lists available at ScienceDirect

Journal of Power Sources

journal homepage: www.elsevier.com/locate/jpowsour

Short communication

Controlled synthesis of α-Fe_2O_3 nanostructures and their size-dependent electrochemical properties for lithium-ion batteries

Yanna NuLi[a,b], Rong Zeng[a], Peng Zhang[a], Zaiping Guo[a,*], Huakun Liu[a]

[a] Institute for Superconducting and Electronic Materials, University of Wollongong, Wollongong, NSW 2522, Australia
[b] Department of Chemical Engineering, Shanghai Jiao Tong University, Shanghai 200240, PR China

ARTICLE INFO

Article history:
Received 19 December 2007
Received in revised form 13 February 2008
Accepted 4 March 2008
Available online 18 March 2008

Keywords:
Iron oxide
Hydrothermal method
Nanostructures
Size-dependent
Anode materials
Lithium-ion batteries

ABSTRACT

Highly crystalline hematite α-Fe_2O_3 nanostructures were selectively synthesized by a simple hydrothermal method. By carefully tuning the concentration of the reactants, reaction time and pressure, a series of α-Fe_2O_3 nanocuboids, nanospheres, nanosheets, nanorods and nanowires can be obtained. Based on the evidence of electron microscope images, a formation mechanism for nanowire-structured hematite is proposed. The electrochemical performance of these hematite nanostructures as anode materials for lithium-ion batteries was further evaluated by cyclic voltammetry, electrochemical impedance and charge–discharge measurements. It was demonstrated that both the morphology and the particle size have an influence on the performance. The results showed that the nanospheres displayed the highest discharge capacity and superior cycling reversibility, which may result from the high surface area and small and uniform grain size.

1. Introduction

It is well known that particle size is an important parameter that strongly influences the properties of powders, especially when the particle size is decreased to the nanometer scale. Three-dimensional (3D) nanomaterials, two-dimensional (2D) layered nanostructures and one-dimensional (1D) nanorods, nanowires and nanotubes have attracted much attention because of their unique properties and potential applications [1,2]. The main objective of nanoscale science and technology has been to synthesize nanomaterials with controlled size and shape, as well as search for new properties that are not realized in microscale morphologies [3]. Among the various nanomaterials, nanostructured metal oxides play an important role in physics, chemistry and material science [4].

As the most stable iron oxide, hematite (α-Fe_2O_3), based on hexagonal close packing of oxygen with iron in 2/3 of the octahedral vacancies, has been extensively used in the production of pigments, catalysts, gas sensors, magnetic recording media and raw materials for hard and soft magnets, due to its low cost, environmental friendliness and high resistance to corrosion [5]. Furthermore, it has also been shown to act as a rechargeable conversion electrode material that reacts with six Li per formula unit, exhibiting higher capacity than carbonaceous substances (e.g., maximum of 372 mAh g^{-1} for graphite) used currently in commercial lithium-ion batteries. A mechanism for the reduction and oxidation of metal nanoparticles, accompanied by the formation and decomposition of Li_2O has been proposed [6]. Iron oxides with large particles have been considered too difficult to be used anode materials for lithium-ion batteries due to their irreversible phase transformation during the reaction [7]. There have been reports, however, on the effects of particle size on the lithium reaction with α-Fe_2O_3, which reached the conclusion that nano-α-Fe_2O_3 has better electrochemical performance than micro-sized α-Fe_2O_3 [8–10].

Because of its excellent properties, considerable efforts have been focused on the properties and synthesis of hematite nanomaterials with controllable size and shape [11], such as nanocrystals [12], nanoparticles [13], nanocuboids [14], nanospindles [15], nanoflakes [16], nanorods [17], nanowires [18], nanobelts [19] and nanotubes [20]. Several methods, such as a template method [21], a sol–gel strategy [17], gas–solid reaction techniques [22] and a hydrothermal approach [20,23] have been developed for the synthesis of hematite nanostructures.

Among the methods mentioned above, hydrothermal synthesis has been shown to be advantageous over other methods in terms of homogeneous nucleation and grain growth of hematite nanocrystals [24]. It has been shown that the preparation conditions, such as concentrations, reaction temperature and reaction time are the main factors in determining the structures and morphologies of the α-Fe_2O_3 nanocrystals [25–27]. Nevertheless, it still remains a

* Corresponding author. Tel.: +61 2 4221 5727; fax: +61 2 4221 5731.
E-mail address: zguo@uow.edu.au (Z. Guo).

0378-7753/$ – see front matter © 2008 Elsevier B.V. All rights reserved.
doi:10.1016/j.jpowsour.2008.03.004

challenge to develop simple hydrothermal approaches to synthesize α-Fe_2O_3 nanostructures with tunable sizes and shapes, which will facilitate our understanding of the size-dependent properties of α-Fe_2O_3.

Herein, we describe an easy route to synthesize α-Fe_2O_3 nanocuboids, nanospheres, nanosheets, nanorods and nanowires via a low-temperature hydrothermal method and report on a study of their properties as attractive anode materials for lithium-ion batteries. Poly(ethylene glycol), with an average molecular weight of 600, was employed as a soft template. PEG is a typical non-toxic, non-immunogenic, non-antigenic and protein-resistant polymer reagent with long polymer chains [28], and the PEG-600 used here plays multiple roles in the synthesis process. It acts as a coordination and linking reactant, as a stabilizer, and as a structure-directing agent [29]. By changing the concentration of the reactants, reaction time and pressure, highly crystalline nanocuboids, nanospheres, nanosheets, nanorods and nanowires can be obtained. Their shape-dependent electrochemical properties as anode materials for lithium-ion batteries have been systematically investigated, using cyclic voltammetry, electrochemical impedance and galvanostatic methods. It was found that as-prepared nanospheres, characterized by uniform size and shape with a high specific surface area, exhibited superior electrochemical activity, with an initial discharge capacity of 1248.1 mAh g^{-1} and capacity retention of 61.1% after 30 cycles at an ambient temperature.

2. Experimental

2.1. Preparation of α-Fe_2O_3 nanomaterials

All the chemical reagents were analytically pure and used without further purification. The α-Fe_2O_3 nanomaterials were prepared by a PEG-precursor route. In a typical experimental procedure, an aqueous solution of $FeCl_3$ (BDH Laboratory Supplies, England) was added dropwise to PEG-600 (Aldrich) methanol solution with equivalent molar number under continuous stirring at room temperature to obtain a homogeneous solution. The solution was kept at 50 °C for 12 h to form crystals, which were collected as precursors. Stoichiometric proportions of the precursors and NaOH aqueous solution (4 M) were added under stirring to a Teflon-lined autoclave, which was filled to one-third by volume. The autoclave was sealed, heated to 160 °C, and maintained at this temperature in an oven for a given period (shown in Table 1). After the reactions, the autoclaves were cooled down naturally. The resulting products were separated by centrifugation, washed with ethanol and distilled water, and then dried under vacuum at 80 °C for 4 h. The detailed preparation conditions of the formed powders are shown in Table 1.

Here, the reaction process of Fe_2O_3 may be similar to that of MnO_2 synthesized using $MnSO_4$, PEG-6000 and NaOH [29]. Fe^{3+} might produce a relatively stable complex once PEG-600 has been added into the aqueous solution of $FeCl_3$. Then, $Fe(OH)_3$ was precipitated after mixing with NaOH. At auto-generated vapour pressure and high temperature, Fe_2O_3 was obtained by reaction with oxygen in air. At the same time, PEG-600 was pyrolyzed to form low-molecular-weight products [30]. Although the exact mechanism is not clear to date, it is reasonable to believe that the PEG-600 mainly controls the size of the as-synthesized crystallites. The chemical equation for this reaction could be expressed as follows:

$$[(FeCl_3)(PEG\text{-}600)(H_2O)] + O_2 + OH^- \rightarrow Fe_2O_3$$

Table 1
Experimental condition for the preparation of the α-Fe_2O_3 nanomaterials

Sample no.	The concentration of PEG-600 (mol L^{-1})	The concentration of $FeCl_3$ (mol L^{-1})	The capacity of autoclave (mL)	Reaction time (h)
1	0.4	1	15	12
2	0.4	1	15	24
3	1	1	15	24
4	1	1	15	48
5	1.5	1	50	24
6	2	1	15	24
7	2	2	15	24
8	2	4	50	24

2.2. Sample characterizations

X-ray powder diffraction (XRD) analysis was conducted on a Philips 1730 X-ray diffractometer using Cu Kα radiation (λ = 1.54056 Å) with 2θ ranging from 20° to 80° to analyse the structure of the resultant products. A JEOL JSM 6460A scanning electron microscope (SEM) was employed to examine the morphology.

For electrochemical measurements, a typical slurry was obtained by grinding a mixture of α-Fe_2O_3, carbon black and poly(vinylidene fluoride) (PVDF) dissolved in *N*-methyl-2-pyrrolidinone (NMP) with a weight ratio of 70:15:15. It was then spread onto a piece of copper foil (1 cm^2) to form an electrode. After the electrode was dried at 100 °C for 4 h under vacuum, it was compressed at a rate of about 150 kg cm^{-2} and then weighed. The cells were assembled in an argon-filled glove box (Mbraun, Unilab, Germany). The charge–discharge measurements were examined via CR2025 coin-type cells with lithium metal counter electrode, Celgard 2400 membrane separator and electrolyte of 1 M $LiPF_6$ in a mixture of ethylene carbonate (EC) and dimethyl carbonate (DMC) (1:1 by volume) at an ambient temperature on a multi-channel battery cycler in the voltage range between 0.01 V and 3.0 V at a current density of 20 mA g^{-1}. Cyclic voltammetry (CV) and electrochemical impedance measurements were performed on three-electrode cells with lithium foils both as the counter and reference electrodes using a CHI instrument. The scanning rate for CV was 0.1 mV s^{-1} and the amplitude of the ac voltage in impedance measurements was 5 mV over the frequency range between 10^5 Hz and 0.1 Hz. The electrochemical impedance measurements were performed at the open-circuit voltage (OCV) before and after the CV experiments.

3. Results and discussion

Fig. 1 shows the X-ray diffraction patterns of as-synthesized powders prepared using the hydrothermal method under different conditions. It can be observed that the positions of the characteristic peaks of the products are consistent with the standard values for the hexagonal α-Fe_2O_3 phase (JCPDS number 33-0664),

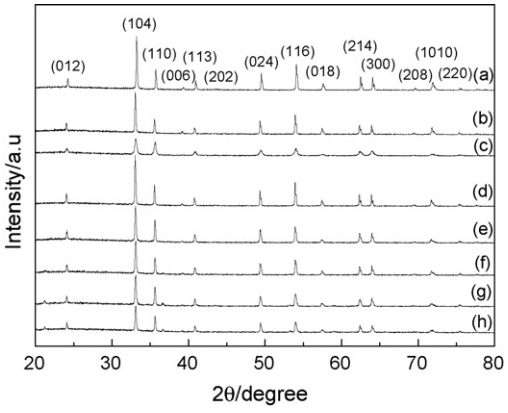

Fig. 1. XRD patterns of as-prepared α-Fe_2O_3 samples: (a) 1, (b) 2, (c) 3, (d) 4, (e) 5, (f) 6, (g) 7 and (h) 8.

Fig. 2. SEM images of as-prepared α-Fe_2O_3 samples: (a) 1, (b) 2, (c) 3, (d) 4, (e) 5, (f) 6, (g) 7 and (h) 8.

whereas the peak intensity differs from one material to the other. The peak intensities of the (1 1 6) diffraction peak in the patterns of Samples 1, 2 and 4 were relatively higher than for the other samples. Among them, the peak intensity of Sample 1 was the strongest, indicating its highly crystalline structure. On increasing the reaction time to 24 h (Sample 2), the intensity of the diffraction peaks was decreased, suggesting that a smaller crystalline size had resulted from a dissolution process over the longer time [31]. On increasing the concentration of PEG-600 from 0.4 M to 1 M and maintaining the time at 24 h, an obvious broadening of peaks for Sample 3 was observed, probably indicating a very fine crystalline size produced by the decomposition process. When the reaction time was increased to 48 h (Sample 4), the intensity of diffraction peaks was remarkably increased, due to the growth

of crystallite over the longer reaction time. However, the relative intensity of the peaks for Samples 5–8 gradually decreased when the concentration of $FeCl_3$ or PEG-600 was increased, indicating that the crystal size became smaller.

Although the XRD patterns of the products only displayed a highly crystalline structure with no indication of the presence of carbon in the products, it is possible that carbon may have been generated by the pyrolysis of excessive PEG-600, if the ratio of PEG-600 to $FeCl_3$ in the precursors was raised or the reaction time was maintained for longer periods [32]. Thus, the ratio of reagents and the reaction time must be carefully controlled.

To obtain a better understanding of the formation and evolution of the shapes of α-Fe_2O_3 nanomaterials, the products under different reaction conditions were collected for SEM investigation. Fig. 2 shows representative images of the samples. It can be seen that powders prepared under different conditions had very different particle shapes and sizes. The main particle shapes were cuboids for Samples 1, 2, 4 and 5, spheres for Sample 3, sheets for Sample 6, rods for Sample 7 and wires for Sample 8, respectively. First, a reaction time-dependent morphology evolution study was conducted. As shown in Fig. 2(a), the product obtained after a 12-h reaction (Sample 1) mainly contained nanocuboids with a diameter of about 3–6 μm and a thickness of about 700 nm. On prolonging the reaction time to 24 h (Sample 2), most of the nanocuboids became thinner, although the size exhibited little change, as shown in Fig. 2(b). Moreover, it was found that the concentration of PEG-600 and $FeCl_3$ had some effect on the particle size and shape, apart from the reaction time. Fig. 2(c) is an SEM image of the Sample 3 obtained when the concentration of PEG-600 increased from 0.4 M to 1 M, which shows that the sample is composed of spheres with typical diameters of about 200 nm. As the reaction time was prolonged, the size of the nanostructures grew gradually and the morphology became nanocuboid again. When it was increased to 48 h (Sample 4), Fig. 2(d) shows that this sample eventually contained no remaining spherical particles and the sample was entirely composed of plate-like nanocuboids with sizes of about 2–5 μm and a thickness of about 500 nm. However, the particles for the Sample 5 prepared using PEG-600 at 1.5 M concentration and an autoclave with 50 mL capacity became smaller and thinner, as shown in Fig. 2(e). On increasing the concentration of PEG-600 to 2 M and using a 15-mL autoclave (Sample 6), a sheet-like morphology was observed, as in Fig. 2(f), and the thickness was close to 100 nm, suggesting that a higher pressure encouraged a smaller crystalline size. With a further increase in the concentration of $FeCl_3$ to 2 M (Sample 7), some nanorods with diameters of about 200 nm and lengths ranging from 500 nm to 1.5 μm were observed, as shown in Fig. 2(g). It is reasonable to believe that the nanorods were formed at a result of the curliness of some thin nanosheets. Sample 8 resulted from further increasing the concentration of $FeCl_3$ to 4 M and using an autoclave with bigger capacity. Fig. 2(h) shows that the product at this stage consists of nanowires with diameters of approximately 100 nm and lengths of about 2 μm. There seemed to have been remarkable preferential coalescence directions for oriented aggregation, resulting in the formation of nanowires. The above results indicated that the capacity of the autoclave, viz. the pressure, had effects on the particle size and shape of the powders, but that the effects of the concentration of reactants and reaction time were more important. It was also observed that the aspect ratio of the nanowires could be tuned by adjusting these parameters.

Based on the above evidence on the evolution of the morphology and its dependences, a possible formation process for the nanostructures can be proposed. Under hydrothermal conditions, nuclei form quickly, followed by the growth of the nuclei into nanocuboid crystals. Then, secondary nucleation occurs on the edges and surfaces of these nanocuboid crystals. This takes place by "dissolution"

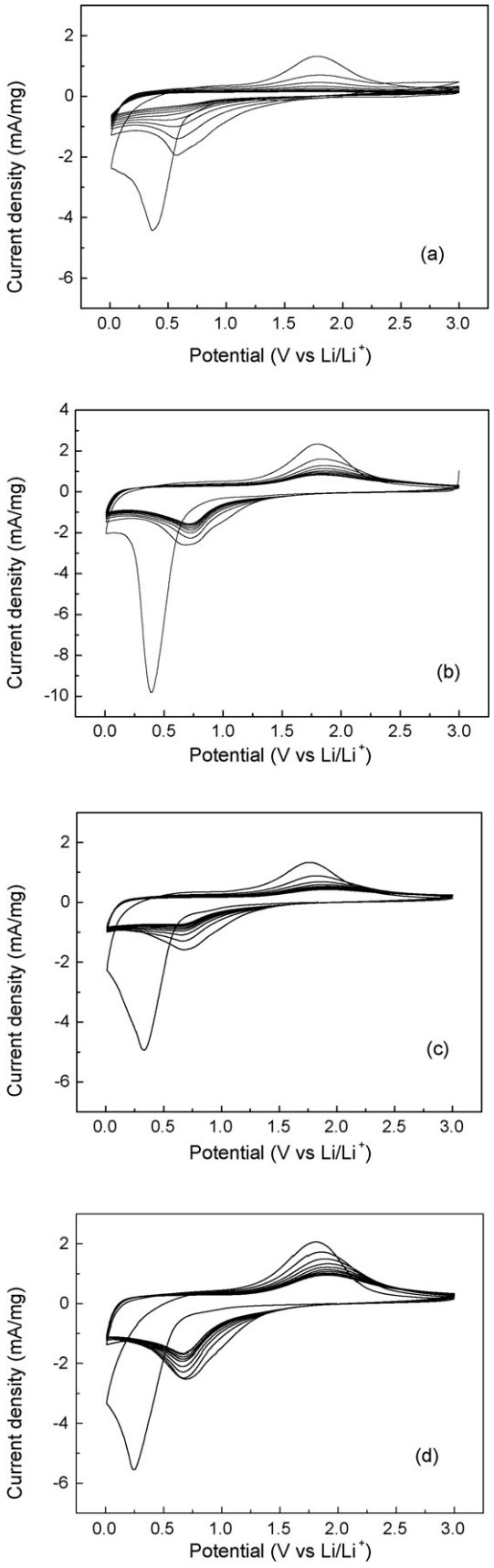

Fig. 3. Cyclic voltammograms of samples: (a) 1, (b) 3, (c) 6 and (d) 8.

of the nanocuboid from the tips toward the interior along the long axis, via spherical, sheet-like and rod-like nanocrystals, until nanowires are formed. Nanosheets tend to curl to form rods, and then wires are formed on increasing the concentration of precursors through a rolling mechanism [33]. Although the formation process of the nanowires has been deduced, the intrinsic cause of the shape transformation from spheres to nanocuboids is still unclear. However, it is interesting that the spheres can evolve into nanowires, and the particle size of the samples was clearly changed by changing the concentration of reagents and the reaction time, suggesting that the shape and size of the nanostructures can be effectively adjusted. To the best of our knowledge, this is the first report about the occurrence of spheres during the formation process from nanocuboids to wires.

Fig. 3(a)–(d) shows cyclic voltammograms of Samples 1, 3, 6 and 8 (representative nanocuboids, nanospheres, nanosheets and nanowires), respectively. In the cathodic process of the first cycle, an obvious peak located at about 0.4 V was observed, which shifted to higher potential in the subsequent reduction process. This can be attributed to the reduction of Fe^{3+} to Fe^0 [9,21] and to some irreversible reaction of the electrolyte [34]. Meanwhile, one main peak with lower intensity was recorded at about 1.8 V in the anodic process, corresponding to the oxidation of Fe^0 to Fe^{3+}. The irreversible capacity might be originated from the decomposition of the electrolyte and subsequent formation of an organic layer deposited at the surface of the particles. Furthermore, a capacity loss takes place during the transformation of Fe^0 to Fe^{3+} due to some thermodynamically impossible extraction of Li from Li_2O [21]. During the subsequent cycles, the curves differ considerably from the first, and the cathodic peak shifts to lower potential and the anodic peak to higher potential, suggesting drastic, lithium-driven, structural or textural modifications [6]. Moreover, the gradually decreasing peak intensity indicated that the capacities could gradually decrease with increasing cycle number.

It can be seen that in the first cycle, the current densities for the nanospheres are larger than those for the other three materials, revealing higher capacity and faster kinetics for the transformation in the nanospheres. In addition, in comparison with the gradually decreasing current densities for the other three materials, the shape of the CV curves in the following cycles remained similar to that of the fourth cycle, showing more reversible reduction and oxidation in the nanospheres.

Fig. 4(A) and (B) presents typical Nyquist plots obtained before and after the CV experiments for Samples 1, 3, 6 and 8. The plots are similar to each other in shape, with a semicircle appearing in the high frequency domain and a straight line in the low frequency region. Comparing the results shown in (A) and (B), it can be seen that the semicircle for every sample became smaller after the CV experiments, suggesting less resistance after several CV cycles. Before the CV experiments, the semicircle for the nanospheres indicated the lowest resistance (ca. 220 $\Omega\,cm^2$). The sequence of resistances at that point was nanowires < nanosheets < nanocuboids. However, the semicircle for the nanowires became the lowest after the CV measurements, so that the resistance value was only 60 $\Omega\,cm^2$. This indicated that the nanowires could exhibit better cycling performance after several cycles.

Fig. 5 shows the discharge curves of the nanocuboids, nanospheres, nanosheets and nanowires during the first and fifth cycles. In the discharge curve of the first cycle, there were a weak potential slope located at 1.2–1.0 V and an obvious potential plateau at 0.9–0.8 V, corresponding to the reaction processes of the electrolyte and of α-Fe_2O_3 with lithium, respectively. During the fifth cycle, only one discharge slope was observed in the range of 1.0–0.9 V, with a decrease in the discharge capacity. Among the four samples, the nanospheres exhibited

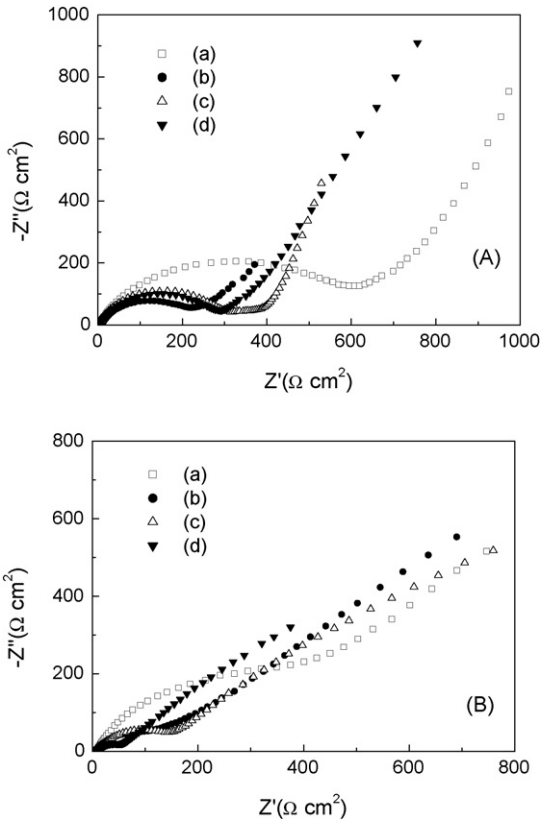

Fig. 4. Electrochemical impedance results obtained (A) before and (B) after the CV experiments for samples: (a) 1, (b) 3, (c) 6 and (d) 8.

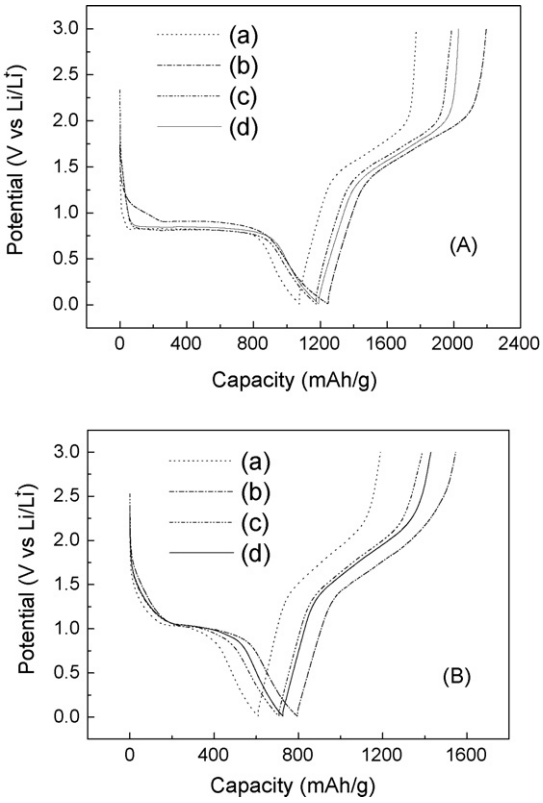

Fig. 5. The (A) first and (B) fifth charge–discharge curves of samples: (a) 1, (b) 3, (c) 6 and (d) 8.

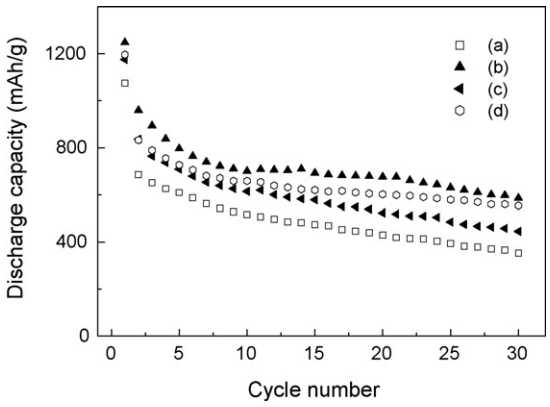

Fig. 6. The discharge capacity vs. cycle number curves of Samples (a) 1, (b) 3, (c) 6 and (d) 8.

the highest discharge capacity, which was 1248.1 mAh g^{-1} for the first cycle and 795.8 mAh g^{-1} for the fifth cycle. The initial discharge capacities of the four materials were ordered as follows: nanospheres > nanowires > nanosheets > nanocuboids and the initial charge–discharge efficiencies were 75.9%, 70.8%, 69.1% and 60.5%, respectively. Moreover, the discharge curve of the nanospheres exhibited a higher discharging voltage than those of the other materials, indicating high power output behavior. There was no doubt that the electrochemical performance of the samples is related to the size effect.

It is well known that a large surface area is important for the improvement of reaction performance, in terms of the introduction of lithium ions into the holes in the hematite surface. The capacity and affinity will be greatly enhanced when the surface area is high, since the diffusion lengths of the lithium ions are greatly shortened. Therefore, the materials with the smallest size and highest surface area would exhibit the highest discharge capacity [35]. Herein, we found that nanowires showed higher discharge capacity than nanosheets and nanocuboids. However, the discharge capacity for the nanospheres was the highest, probably due to the high uniformity and good dispersion, as shown in Fig. 2.

Fig. 6 presents the cycling behavior of nanocuboids, nanospheres, nanosheets and nanowires. All the materials showed large reversible capacities in the initial 10 cycles. However, the capacities then gradually decreased, and the rate of the capacity decay from the 1st to the 10th cycle was much higher than that from the 10th to the 30th cycle. For the representative samples, the nanospheres maintained a capacity of 585.6 mAh g^{-1} after 30 cycles, corresponding to about 61.1% of the second capacity, while nanowires, nanosheets and nanocuboids showed about 66.5%, 53.2% and 51.5% of the second capacity, respectively. This indicated that the capacity retention was ordered as nanowires > nanospheres > nanosheets > nanocuboids. Obviously, the nanowires could recover some of its capacity after long-term cycling, indicating that orderly arrangements of 1D nanostructures exhibit better capacity retention. This may relieve the stress caused by volume change during the numerous charge–discharge cycles, and suppress the degradation of the material. It was demonstrated that both the morphology and the particle size have an influence on the cycle life. Increased uniformity of the nanowires should lead to superior electrochemical performance.

4. Conclusions

Herein, we reported a feasible and controllable synthesis method for cubic, spherical, sheet-like, rod-like and wire-like hematite nanocrystals by a convenient hydrothermal method. Various experimental conditions, including the concentration of the reactants, the reaction time and the pressure, for the growth of nanocrystals were investigated. It was concluded that the solution conditions had particular effects on the particle size and shape of the powders. A possible formation mechanism for these nanostructures was proposed in accordance with the morphology investigations. Furthermore, the size-dependent electrochemical properties were investigated. Probably due to the fine particle size and large surface area, α-Fe_2O_3 nanospheres showed better electrochemical performance, with a high initial capacity of 1248.1 mAh g^{-1} and a good capacity retention of 61.1% after the 30th cycle at 20 mA g^{-1}.

Acknowledgement

This work is financially supported by the Australian Research Council through a Linkage Project (LP0775456).

References

[1] R.F. Service, Science 309 (2005) 95.
[2] X.G. Peng, L. Manna, W. Yang, J. Wickham, E. Scher, Nature 404 (2000) 59.
[3] Y. Sue, B. Mayers, Y. Xia, Adv. Mater. 15 (2003) 641.
[4] G.R. Patzke, F. Krumeich, R. Nesper, Angew. Chem. Int. Ed. 41 (2002) 2446.
[5] C. Gong, D. Chen, X. Jiao, Q. Wang, J. Mater. Chem. 12 (2002) 1844.
[6] P. Poizot, S. Laruelle, S. Grugeon, L. Dupont, J.-M. Tarascon, Nature 407 (2000) 496.
[7] M. Pernet, P. Strobel, B. Bonnet, P. Bordet, Y. Chabre, Solid State Ionics 66 (1993) 259.
[8] D. Larcher, C. Masquelier, D. Bonnin, Y. Chabre, V. Masson, J.B. Leriche, J.M. Tarascon, J. Electrochem. Soc. 150 (2003) A133.
[9] D. Larcher, D. Bonnin, R. Cortes, I. Rivals, L. Personnaz, J.M. Tarascon, J. Electrochem. Soc. 150 (2003) A1643.
[10] T. Matsumura, N. Sonoyama, R. Kanno, M. Takano, Solid State Ionics 158 (2003) 253.
[11] T. Sugimoto, K. Sakata, J. Colloid Interface Sci. 152 (1992) 587.
[12] S.H. Sun, H. Zeng, D.B. Robinson, S. Raoux, P.M. Rice, S.X. Wang, G.X. Li, J. Am. Chem. Soc. 126 (2004) 273.
[13] H. Deng, X.L. Li, Q. Peng, X. Wang, J.P. Chen, Y.D. Li, Angew. Chem. Int. Ed. 44 (2005) 2782.
[14] S. Hamada, E. Matijivic, J. Colloid Interface Sci. 84 (1981) 274.
[15] M. Ozaki, S. Kratohvil, E. Matijevic, J. Colloid Interface Sci. 102 (1984) 146.
[16] Y.W. Zhu, T. Yu, C.H. Sow, Y.J. Liu, A.T.S. Wee, X.J. Xu, C.T. Lim, J.T.L. Thong, Appl. Phys. Lett. 87 (2005), 023 103.
[17] K. Woo, H.J. Lee, J.P. Ahn, Y.S. Park, Adv. Mater. 15 (2003) 1761.
[18] R.M. Wang, Y.F. Chen, Y.Y. Fu, H. Zhang, C. Kisielowski, J. Phys. Chem. B 109 (2005) 12245.
[19] X.G. Wen, S.H. Wang, Y. Ding, Z.L. Wang, S.H. Yang, J. Phys. Chem. B 109 (2005) 215.
[20] C.J. Jia, L.D. Sun, Z.G. Yan, L.P. You, F. Luo, X.D. Han, Y.C. Pang, Z. Zhang, C.H. Yan, Angew. Chem. Int. Ed. 44 (2005) 4328.
[21] J. Chen, L.N. Xu, W.Y. Li, X.L. Gou, Adv. Mater. 17 (2005) 582.
[22] L. Liu, H.Z. Kou, W.L. Mo, H.J. Liu, Y.Q. Wang, J. Phys. Chem. B 110 (2006) 15218.
[23] J. Wan, X. Chen, Z. Wang, X. Yang, Y.T. Qian, J. Cryst. Growth 276 (2005) 571.
[24] K. Byrappa, T. Adschiri, Prog. Cryst. Growth Char. Mater. 53 (2007) 117.
[25] Z. Jing, S. Wu, Mater. Lett. 58 (2004) 3637.
[26] Y. Zheng, Y. Cheng, Y. Wang, F.J. Bao, Cryst. Growth 284 (2005) 221.
[27] G.S. Li, R.L. Smith Jr., H. Inomata, K. Arai, Mater. Res. Bull. 37 (2002) 949.
[28] J.M. Harris, in: J.M. Harris (Ed.), Poly(ethylene glycol) Chemistry, Biotechnical and Biomedical Application, Plenum Press, New York, 1992 (Chapter 1).
[29] F.Y. Cheng, J. Chen, X.L. Gou, P.W. Shen, Adv. Mater. 17 (2005) 2753.
[30] S. Han, C. Kim, D. Kwon, Polymer 38 (1997) 317.
[31] Ch.J. Jia, L.D. Sun, Zh.G. Yan, L.P. You, F. Luo, X.D. Han, Y.Ch. Pang, Z. Zhang, Ch.H. Yan, Angew. Chem. Int. Ed. 44 (2005) 4328.
[32] H. Bi, Q.W. Chen, T. Sun, Solid State Commun. 141 (2007) 573.
[33] Y.R. Hacohen, E. Grunbaum, R. Tenne, J. Sloan, J.L. Hutchison, Nature 395 (1998) 336.
[34] X.H. Huang, J.P. Tu, C.Q. Zhang, J.Y. Xiang, Electrochem. Commun. 9 (2007) 1180.
[35] S.Y. Zeng, K.B. Tang, T.W. Li, J. Colloid Interface Sci. 312 (2007) 513.